applied sciences

MDPI

Article

A Comparative Study in Forming Behavior of Different Grades of Steel in Cold Forging Backward Extrusion by Integrating Artificial Neural Network (ANN) with Differential Evolution (DE) Algorithm

Praveenkumar M. Petkar [1], Vinayak N. Gaitonde [1,*], Vinayak N. Kulkarni [1], Ramesh S. Karnik [2] and João Paulo Davim [3]

[1] School of Mechanical Engineering, KLE Technological University, Hubballi 580031, Karnataka, India
[2] Department of Electrical and Electronics Engineering, KLE Technological University, Hubballi 580031, Karnataka, India
[3] Department of Mechanical Engineering, University of Aveiro, Campus Santiago, 3810-193 Aveiro, Portugal
* Correspondence: vngaitonde@kletech.ac.in or gaitondevn@yahoo.co.in; Tel.: +91-9480556558

Abstract: The cold forging backward extrusion is employed to produce parts that are characterized by better mechanical strength. However, in this process, punches are often prone to breakages because of the large forces encountered in deforming the steel billets. The service life of the punches is affected majorly by the geometrical attributes, the type of steel undergoing deformation, and hence the present investigation focuses on the applications of natural computing algorithms such as artificial neural network (ANN) and differential evolution (DE) optimization algorithm to study the differential influence on the forming behavior of different grades steel and enhance the punch service life. The AISI steel grades, such as AISI 1010, 1018, and 1045, employed extensively in the production of automotive components, have been compared in terms of forming behavior, such as effective stress, strain, strain rate, and punch force. The multi-layer feed-forward ANN architecture was utilized for process modeling with forming responses of finite element (FE) simulations that are strategically planned through the design of experiments (DoE) approach. Considerable variations were found for the effective stress and punch force amongst the steels, while marginal deviations were observed for effective strain and strain rates. Confirmatory experiments were conducted to validate the results of optimal combinations obtained through the DE optimization technique, and the deviations were observed to be in the acceptable range. The cold forging backward extruded components have also been examined for better mechanical soundness through microstructure and micro-hardness analysis that clearly revealed the mechanical integrity and strength enhancement within the forged components. The proposed study would assist the industries engaged in the production of cold-forged steel components in determining the appropriate values of variables to minimize the forming responses and, thus, help in enhancing the life of the tooling.

Keywords: cold forging backward extrusion; finite element simulation; design of experiments; artificial neural network modeling; differential evolution optimization; micro-hardness

Citation: Petkar, P.M.; Gaitonde, V.N.; Kulkarni, V.N.; Karnik, R.S.; Davim, J.P. A Comparative Study in Forming Behavior of Different Grades of Steel in Cold Forging Backward Extrusion by Integrating Artificial Neural Network (ANN) with Differential Evolution (DE) Algorithm. *Appl. Sci.* **2023**, *13*, 1276. https://doi.org/10.3390/app13031276

Academic Editor: Gaige Wang

Received: 2 December 2022
Revised: 11 January 2023
Accepted: 16 January 2023
Published: 18 January 2023

1. Introduction

The cold forging process can manufacture parts with near-net shapes for greater strength and accuracy with less waste compared to hot forging [1–3]. The cold forging manufacturing process is mainly employed to produce the metal parts featured as less mass-enabled stronger ones. The present trend in manufacturing by the metal forming process seeks three critical aspects to be embedded in the product; better accuracy/precision, surface quality, and mechanical properties [4]. The cold forging process has been proven to be a favorable contender among other manufacturing processes for the production of such parts featured with precision, strength, and lightweight [5]. Moreover, the automotive and aerospace domain will be significantly affected by environmental aspects in the coming decade, with new norms affecting majorly on power-train [6,7]. Cold forging qualifies these capabilities, and the parts produced out of cold forging are classified for superior mechanical properties induced by the process. Such typical parts are being employed where the strength becomes pivotal, for example, components of engines, power transmission, and housings, etc., [8–10]. In order to improve the mechanical stiffness of a component, cold forging was employed instead of the fine blanking process in an automotive part [11]. Despite offering distinct advantages over hot forging or other manufacturing processes, cold forging technology is still a challenge to the industry. Higher process force requirements and frequent die failures due to wear and fatigue can cause trouble when working out a cold forging cycle [12,13].

The cold forging process comprises forward extrusion, backward extrusion, and combined forward–backward extrusion, and various axi-symmetrical configurations are possible depending on the final geometry to be achieved. The cold forging backward extrusion is employed for producing cup-shaped axi-symmetrical parts used in automobile and aerospace applications [14]. Since the huge amount of forces required to deform the metal in cold forging backward extrusion, the die elements are often subjected to severe stresses and are prone to failures [15–17]. Therefore, the industry must pay close attention to economic viability to produce the components. The cold forging backward extrusion is a relatively complex process as the material's flow pattern depends on several factors, such as the frictional conditions at the work–piece/tooling interface, the geometry of the billet (pre-form), die elements, the material type, and the percentage reductions [18]. Due to the complexity of the analysis and many process variables, it is not easy to estimate the forming aspects of a given component [19].

Recent advances in process design and optimization show the extensive use of finite element method (FEM) simulation tools that reduced process development lead time [20]. The finite element technique was used to investigate the complex process design of the cold forging with a floating die to obtain a suitable die velocity, which depends on the contact stress between die and workpiece [21]. Investigations of thermal effects on workpiece optimization for complex geometries like propeller hubs were carried out using FE simulation technique [22]. The effect of mechanical and thermal loads on the components' accuracy produced through the cold forging process with due consideration on spring-back was studied by Jun et al. [23] using FEM. Since many process variables are included in the cold forging process, researchers have contributed in developing predictive models by optimizing process variables in the cold forging domain using meta-heuristic techniques along with FEM. Further, the geometry of the work part (pre-form) influences the metal fill pattern in the die cavity to achieve the final configuration. Sedighi et al. [24] illustrated the pre-form optimization using a neural network and genetic algorithm that resulted in a 50% reduction of the forging force. Artificial intelligence (AI) techniques have been utilized and compared in the design of the predictive tool for forging operations that comprise of input–output relationships, where the focus was on minimizing operational loads, material consumption, and energy without affecting the quality of the part being forged [25].

The present paper proposes to integrate two natural computing algorithms, the artificial neural network (ANN) and differential evolution (DE) algorithm, to model and optimize the cold forging process of AISI steel grades such as AISI 1010, 1018, and 1045. The ability to capture highly non-linear relations between several process parameters and responses of ANN makes it suitable to model the cold forging process. Once properly trained with experimental input–output data set, known as training patterns, ANN can further generalize the process behavior for any new data points.

DE is a new branch of natural computing optimization algorithms. DE is real-coded population-based search algorithm and has proven to be highly efficient in providing global optimal solutions. The DE algorithm is based on the creation of new offspring chromosome generation through reproduction involving crossover, mutation, and natural selection. The crossover using the best-fit chromosome improves the DE convergence speed. On the other hand, randomly selected chromosome pairs are employed in the mutation process helps to maintain the population diversity and overcome the destructive crossover. DE exhibits self-tuning property and hence uses few control parameters which are easy to determine for a given problem. The overall DE algorithm is very simple and, hence, easy to develop the program.

The adoption of the cold forging process is limited in industry, mainly because of higher force requirements leading to frequent die failures; particularly, in cold forging backward extrusion, where the punches are more prone to breakages when working out steel as a billet material. Hence, there is a need to adopt a systematic approach to achieve a deeper understanding of the cold forging backward extrusion. Process modeling, along with advanced finite element simulation tools, have relatively more benefits over traditional trial and error methods to analyze the feasibility of the process. Moreover, the study would benefit small and medium-scale industries that cannot afford design and simulation tools to understand the forming behavior of different steels and also to decide upon the optimal parameters for the economic viability of the process. Cold forging is a quite complex process; however, conventional process modeling and optimization methods lack in capturing the non-linearity involved in the process. Therefore, the intent of the work is to build predictive models and optimize the cold forging process using AI techniques. In addition, a comparative study on forming behavior of different AISI steel grades will definitely assist in arriving at the best combinations, which will increase the punch performance.

The investigations on the forming aspects will help industries to reduce development time as well as cost. In the current investigation, a comparative study has been carried out on the forming behavior of different AISI grade steels that emphasizes the role of finite element simulation coupled with differential evolution optimization technique for analyzing the effect of critical geometrical factors: namely, billet size, reduction, punch angle, and land height. As part of experimental validation, an attempt has been made to capture the forming responses, such as forging force, effective strain, strain rate, and stress. Micro-structural observations including micro-hardness studies have also been performed on the cold forged samples to verify the quality of the forgings, confirming the appropriateness of the identified variables and their levels. The effort is mainly focused on the development of a knowledge base for the three different AISI grade steels, namely AISI 1010, AISI 1018, and AISI 1045, through a comparison of forming behavior in cold forging backward extrusion.

2. Method and Materials

The formability of different steel used in manufacturing parts for automobile applications is majorly affected by the billet size and punch geometry in the cold forging backward extrusion. Moreover, these geometrical attributes are dictated by the intended inner configuration of the part, which could be achieved through multiple forging stages. The cold forging backward extrusion is generally utilized for manufacturing closed-end axi-symmetrical hollow parts, and the punch is designed with empirical rules. The strategy for the current research is planned as illustrated in Figure 1, with the design of experiments (DoE) approach for the finite element (FE) simulations and further, the forming responses are utilized for artificial neural network (ANN) process modeling, and later employed for differential evolution (DE) for optimization. Finally, confirmatory experiments were conducted in collaboration with the industry to authenticate the results obtained through the DE technique.

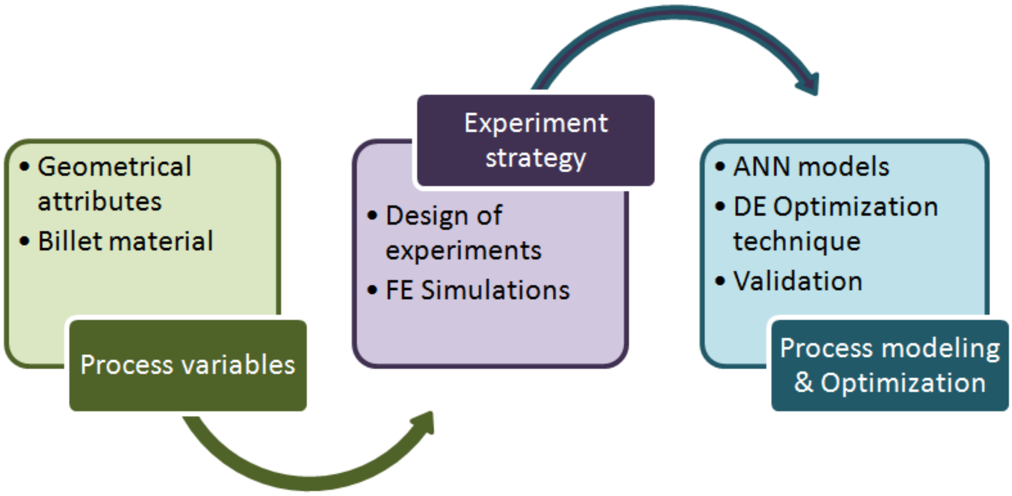

Figure 1. The research approach for the current investigation.

2.1. Materials

Cold forging enables components with process-induced strength and enhanced mechanical properties. The process offers higher strength through the refinement of grain structure, aligning grain orientation with the final configuration of the part. Most of the automotive parts are produced with steel employed for critical applications such as power transmission, joints, and axle assemblies [26,27].

The formability of the steel can be attributed to the carbon content present, which, in fact, is a prime alloying element in the steel. Automotive components are being manufactured extensively with AISI-designated steels; therefore, the steels, namely, AISI 1010, AISI 1018, and AISI 1045, have been selected in the current study. Table 1 illustrates the composition and mechanical properties of these selected steels [28].

Table 1. Chemical composition and mechanical properties of steel grades.

Chemical Composition-Specifications as per BS 970-1955, (Inspected % Weight)				
Elements	AISI 1010	AISI 1018		AISI 1045
C	0.08–0.13 (0.008)	0.15–0.20 (0.180)		0.43–0.45 (0.410)
Si	0.15–0.35 (0.195)	<0.300 (0.190)		<0.300 (0.300)
Mn	0.30–0.60 (0.545)	0.60–0.90 (0.690)		0.60–0.90 (0.710)
P	0.04 Max. (0.013)	0.04 Max. (0.022)		0.04 Max. (0.025)
S	0.05 Max. (0.003)	0.05 Max. (0.09)		0.05 Max. (0.006)
Mechanical Properties				
Tensile strength (MPa) Yield (Ultimate)		180 (325)	220 (410)	310 (565)
Hardness Vickers (Brinell no.)		105 (108)	131 (126)	170 (163)
Reduction area (%)		50	40	40
Elongation (%)		28	25	17
Elastic modulus (GPa)		200	200	200
Bulk modulus (GPa)		140	140	140
Shear modulus (GPa)		80	80	80

2.2. Process Variables and Finite Element Simulations

The geometrical attributes that significantly affect cold forging backward extrusion are billet size, reduction ratio, punch angle, and land height. The levels of the identified factors have been listed in Table 2. The mentioned ranges for the geometrical attributes have been selected based on practical intuition and industry practices [29].

Table 2. Process variables and their levels.

Geometrical Attribute	Designation and Unit	Levels			
		I	II	III	IV
Billet size ratio	z-	0.3	0.6	0.9	1.2
Reduction ratio	r-	0.3	0.4	0.5	0.6
Punch angle	a-deg	160	163	167	170
Land height	h-mm	2.0	2.7	3.3	4.0

The billet size ratio (z) is the ratio of billet diameter (D_0) to billet length (L_0). The billet diameter is fixed at 30 mm owing to practical constraints, and the length is varied from 9–36 mm to get the ratios of 0.3–1.2, as listed in Table 2. The reduction ratio (r) is the ratio of the cross-sectional area difference between the billet and the punch to the billet. Since the billet size is fixed to Ø30 mm, the reduction ratio limits are 0.3, 0.4, 0.5, and 0.6; corresponding punch sizes are Ø25, 23, 21, and 19 mm, respectively. The punch angle (a) is a very important factor that facilitates metal flow during deformation and is decided based on the industry intuition, set to vary from 160–170°. Similarly, land height (h) is varied between 2–4 mm and is crucial because of the friction during metal flow over the punch about the contact area. The cold forging backward extrusion limitation is set either to the ratio ($^{L_i}/_{D_i}$) not exceeding 1.6, where L_i is extruded length and D_i-extruded diameter; otherwise, the bottom thickness of the extruded cup should not be less than 3–5 mm. This is because of the material deformation constraint, and if the bottom thickness falls less by the value mentioned, undue pressure will mount during deformation on the punch by the counter punch (meant for the ejection of the part from the die container), leading to catastrophic failure. For the experimental design, the full factorial design (FFD) strategy [30] is employed with the four factors; each factor is defined at four levels to plan for FE simulations. The three-dimensional (3D) model assembly combinations, as planned with DoE, comprise punch, billet, and die container, and are modeled using SOLIDWORKS software [31]. As the models are cylindrical, assemblies are segmented to a symmetrical plane of 30° in order to reduce simulation time and memory space.

AFDEX software [32] has been utilized, as illustrated in Figure 2, to simulate the process with 3D assembly model combinations that are saved in a stereo lithographic (.stl) format. The models are discretized with the auto-generated meshing option and about 3000–6000 approximately average number of tetrahydron elements were formed. The inputs for forming simulation, such as material and friction models, are selected from the in-built library. The stroke of the press is set so as to confirm the extrusion limit posed by extruded diameter to length ($^{L_i}/_{D_i}$) to 1.6 or cup bottom thickness maintained to 3–5 mm. The average time of simulation varies from 13–18 min, depending on the computer system configuration. Through FE simulations, proper care has been exercised in recording the forming responses for effective stress, strain, strain rate, and punch force for different steels (AISI 1010, 1018, and 1045). The forming responses have been gathered with three to four iterative simulation runs and averaged. Since the AFDEX metal forming simulation software is precisely meant for metal forming processes, the accuracies involved can be justified with that of experimental results.

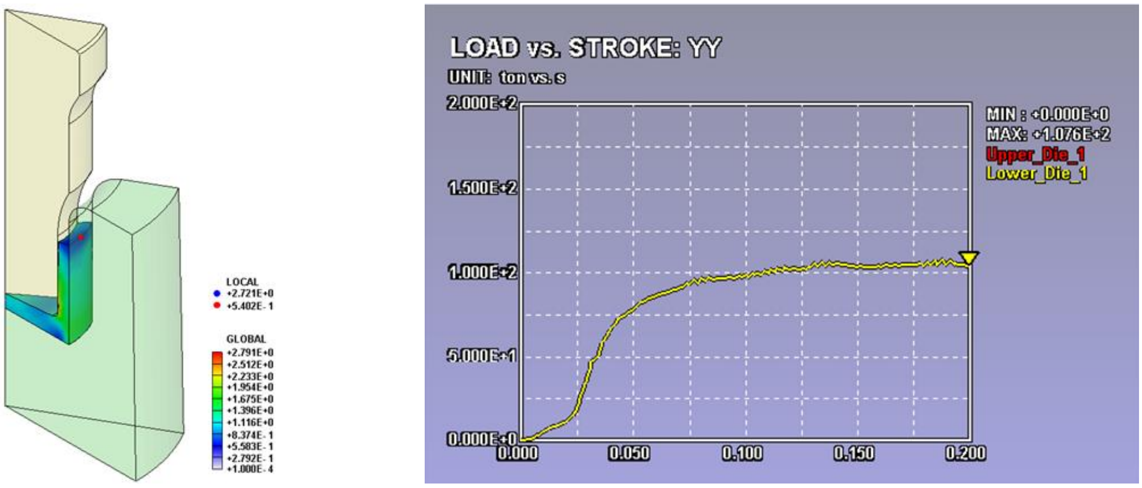

(a) (b)

Figure 2. (**a**) FE Simulation; (**b**) load versus stroke curve to capture maximum punch force.

2.3. Process Modeling and Optimization

In the current investigation, significant geometrical aspects are accounted for the evaluation of forming behavior of AISI steel grades. The input–output data gathered from FE simulations have been utilized for the process modeling using an artificial neural network (ANN), and optimal combinations of control and response factors have been generated through the differential evolution (DE) optimization technique.

2.3.1. ANN Process Modeling

Artificial neural networks (ANN) are interconnected collections of nodes known as neurons. The capability of the ANN is stored in the inter-unit connection weights acquired through a process of learning from training patterns [33]. In the current research, the architecture of the ANN with error back propagation training algorithm was established on a gradient descent with momentum and variable learning rate "traingdx", using MATLAB toolbox [34]. The ANN architecture is depicted in Figure 3.

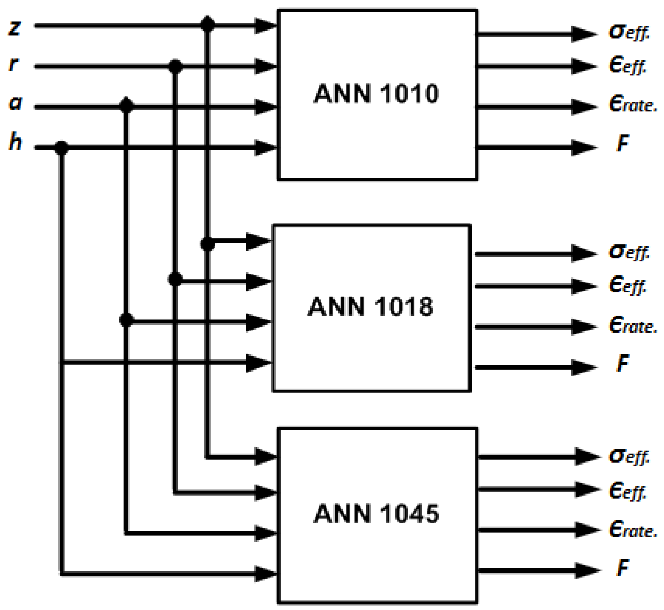

Figure 3. ANN Architecture of current investigation.

The 256 training combinations were used for modeling, out of which 88% were employed for training and 12% were used for testing. The parameters involved in ANN are listed in Table 3. Each neuron in the hidden layers employs a sigmoid activation function, whereas the output layer neurons employ a linear activation function.

Table 3. ANN training parameters.

Particulars	Multi-Layer Feed Forward ANN Model		
	AISI 1010	AISI 1018	AISI 1045
Number of input and output variables	4, 4	4, 4	4, 4
Number of neurons in 1st hidden layer	8	8	8
Number of neurons in 2nd hidden layer	6	6	12
Learning rate (α)	0.1	0.1	0.1
Momentum constant (β)	0.9	0.9	0.9
Learning rate increment	1.05	1.05	1.05
Maximum number of epochs	2500	2500	2500

Every epoch involves 226 (out of a possible 256) patterns to train the ANN, and at the end of every epoch, the mean square error (MSE) is calculated as mentioned below:

$$MSE = \frac{1}{226} \sum_{p=1}^{226} \sum_{k=1}^{4} \left(t_{kp} - O_{kp}\right)^2 \quad (1)$$

where t_{kp} and O_{kp} are the preferred output and realistic output, respectively, of the k^{th} neuron for the p^{th} pattern.

When the desired MSE or the predetermined number of epochs has been reached, the training is concluded. The training was terminated after 2500 epochs, as shown in Figure 4, and the MSE was found within the allowed range, as indicated in Table 4.

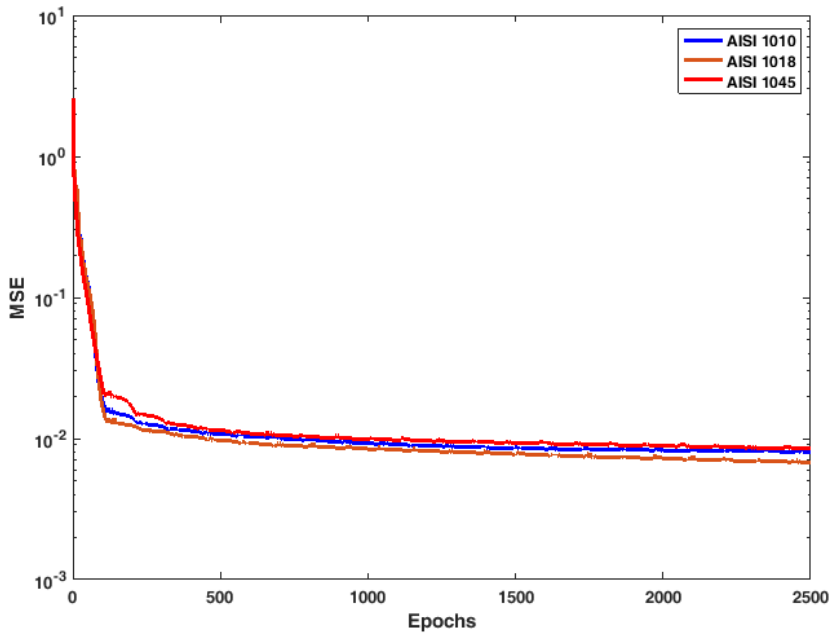

Figure 4. Variation between MSE and the number of epochs of ANN training for AISI 1010, 1018, and 1045 steel.

Table 4. Mean square error (MSE) for different AISI grades steel.

Particulars	MSE at the End of 2500 Epochs
AISI 1010 model	0.00804
AISI 1018 model	0.00679
AISI 1045 model	0.00847

2.3.2. Methodology of DE Optimization

Differential evolution (DE) is a population-based technique that is widely utilized in engineering applications to resolve various optimization challenges [35]. Real-world optimization problems have two fundamental steps: the model construction of the process and solving the optimization model [36]. Optimization problems are always associated with either maximizing or minimizing the effect of the output response factor with input variables.

The function can be represented by $f(x)$ Maximize/Minimize

The DE algorithm consists of a population of size N, and the population matrix can be shown with Equation (2),

$$x^g_{n,\ i} = \left[x^g_{n,\ 1,}\ x^g_{n,\ 2,}\ \ x^g_{n,\ 3,}\ \ \ldots,\ x^g_{n,\ D,}\ \right] \tag{2}$$

where g is the generation, n = 1, 2, 3, ..., N and D is the number of variables.

The initial data of input variables with response factors are to be gathered from the experimentation. The lower and upper limit bounds of solution search space can be used to produce the initial candidate solutions during the initialization phase. The i^{th} chromosome offspring is produced as Equation (3):

$$\begin{gathered} y_{i,j} = x_{i,j} + K\left(x_{best,j} - x_{i,j}\right) + F\left(x_{r1,j} - x_{r2,j}\right) \\ for\ i = 1, 2,\ \ldots N\ and\ j = 1,\ 2,\ \ldots D \end{gathered} \tag{3}$$

K: crossover scale coefficient

F: mutationscale coefficient

r_1 and r_2: random integers in the range [1:N] such that $r_1 \neq r_2$, r_1, $r_2 \neq i$ (distinct and not equal to i)

The selection procedure allows DE to maintain population size in each generation while determining the survival of a target (parent) or a trial (offspring) solution in the subsequent iteration of the search process. Following the formation of the new population in the next generation, repetitive processes of mutation, crossover, and selection are carried out constantly until the termination criteria are satisfied. The selection process of DE is mathematically described as;

$$x_i^{g+1} = \begin{cases} y_i^g\ if\ Fit\ \left(y_i^g\right) \leq Fit\ \left(x_i^g\right) \\ x_i^g\ otherwise \end{cases} \tag{4}$$

For, i = 1, 2, 3 . . . N

Every child will compete against its corresponding parent, and the surviving will all make up the population of parents for the following generation. The fitness value of an individual solution can be determined if the most recent trial vector y_i^g creates an improved fitness value, then the present target vector x_i^g will be substituted by y_i^g in the subsequent iteration.

The FE simulations and DE optimization technique has been employed to avail the optimal combinations of control factors, such as billet size ratio (z), reduction ratio (r), punch angle (a), and land height (h) to yield for lower values of the response factors, effective stress, strain, and punch force, while maximizing strain rate. The objective or fitness function (Fit) of the DE optimization technique is to minimize the Fit subjected to inequality constraints $160 \leq a \leq 170$, $2 \leq h \leq 4$ and therefore determined as shown with Equation (5).

$$Fit = \frac{1}{(\varepsilon_{rate})_n} + \left(\sigma_{eff}\right)_n + \left(\varepsilon_{eff}\right)_n + (F)_n \tag{5}$$

The normalized values for AISI 1010, 1018 and 1045 are expressed in Equations (6)–(8), respectively,

$$\text{AISI 1010} \quad (F)_n = \frac{F}{131}; \left(\sigma_{eff}\right)_n = \frac{\sigma_{eff}}{1050}; \left(\epsilon_{eff}\right)_n = \frac{\epsilon_{eff}}{5.5}; (\epsilon_{rate})_n = \frac{\epsilon_{rate}}{76}; \tag{6}$$

$$\text{AISI 1018} \quad (F)_n = \frac{F}{133}; \left(\sigma_{eff}\right)_n = \frac{\sigma_{eff}}{1060}; \left(\epsilon_{eff}\right)_n = \frac{\epsilon_{eff}}{5.7}; (\epsilon_{rate})_n = \frac{\epsilon_{rate}}{90}; \tag{7}$$

$$\text{AISI 1045} \quad (F)_n = \frac{F}{177}; \left(\sigma_{eff}\right)_n = \frac{\sigma_{eff}}{1230}; \left(\epsilon_{eff}\right)_n = \frac{\epsilon_{eff}}{5.7}; (\epsilon_{rate})_n = \frac{\epsilon_{rate}}{73}; \tag{8}$$

The DE algorithm for all three AISI steel grade materials with 50 chromosomes (population size), 50 maximum generations, crossover coefficient (K) of 0.5, and mutation coefficient (F) of 0.5 has been set and run through the developed MATLAB DE program. The plots for optimal combinations of control factors and responses have been explained in the subsequent Section 3.3.

2.4. Experimental Details

The experiments have been planned with eight combinations of optimal control factors obtained from DE optimization of AISI grade steels, owing to the industry's cost constraints and practical feasibility. The experimental data for forming responses have been gathered with a minimum of five replicates in each combination for AISI 1010 steel, and the same have been represented in Table 5. The punches are manufactured accurately to a tolerance of 0.02 mm with high-speed steel material (S600 BOHLER grade) and heat-treated to 61–63 Rc. The billets were also machined with AISI 1010 steel material, annealed to 108 Hv, and coated with molybdenum disulfide. The punches and billets have been machined on a CNC turning center, and inspected with a micrometer and FARO ARM coordinate measuring machine to substantiate tolerances on GD&T parameters such as concentricity, perpendicularity, and cylindricity. Figure 5 shows the machining operations and inspection performed for the manufacture of punches and billets. The experiments were conducted on a close-frame 600 Ton hydraulic press (Chimaho automation systems).

Table 5. Punch and billet sizes according to DE Optimal control factors for AISI 1010 steel.

Sl. No.	Reduction Ratio (r)	Billet Size Ratio (z)	Punch Diameter (d-mm)	Billet Size (mm)	Punch Angle (a-deg)	Land Height (h-mm)
1	0.3	0.5	25	Ø30 × 15	170	2.0
2	0.3	0.7	25	Ø30 × 21	170	2.0
3	0.4	0.5	23	Ø30 × 15	170	4.0
4	0.4	0.8	23	Ø30 × 24	170	2.6
5	0.5	0.5	21	Ø30 × 15	160	4.0
6	0.5	0.7	21	Ø30 × 21	160	4.0
7	0.6	0.5	19	Ø30 × 15	160	4.0
8	0.6	0.7	19	Ø30 × 21	160	4.0

The billets, after annealing, have been lubricated with MoS_2 powder of 3 µm particle size before placing them in the die cavity to facilitate better deformation. The punches are mounted onto the ram sequentially according to the experimentation order. A master pressure/force gauge of 400 kg/cm^2 capacity has been specifically designed and manufactured. The 250 mm dial size of the master gauge has been exclusively planned to capture the forces at higher resolution and to measure the force with a least count of 0.25% of a full-scale division. The gauge had been connected and integrated with the press during experiments. A high-resolution imaging technique was employed to capture the needle deflection and the readings of the master gauge with a digital single-lens reflex camera (Nikon D5600 DSLR). The experimental process and gauge readings have been recorded, as shown in Figure 6a,b.

Figure 5. Punches and billets preparation (Courtesy: KLE Technological University, Hubballi, India).

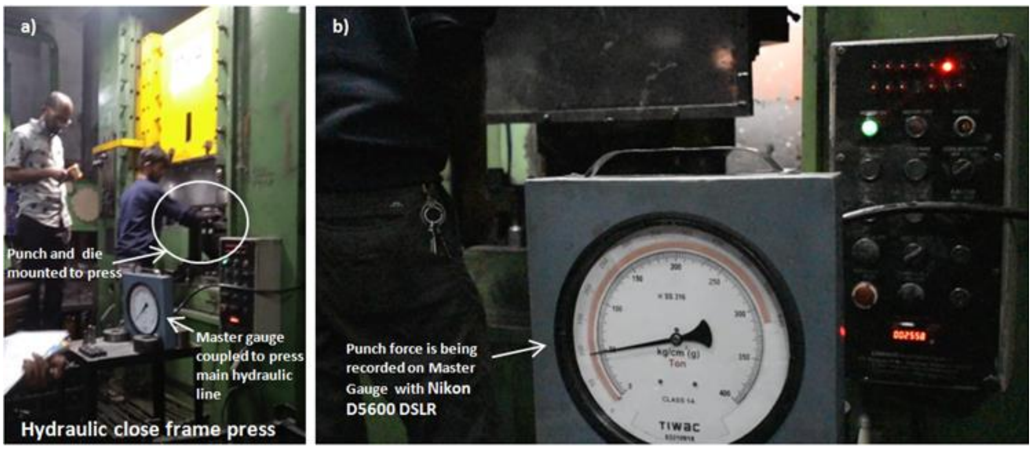

Figure 6. (**a**) Close frame 600 Ton hydraulic press; (**b**) the master gauge and experimental set-up (Courtesy: S. S. Industries, Bangalore, India).

The forged part has been sectioned in the transverse direction to obtain the metallographic examination possible in this section. The slit forged specimen surface is ground with SiC papers and polished with 1 µm diamond paste. Figure 7 depicts the initial state of the raw material (billet), forged, and mid-sectioned parts. Micro-hardness values at cup thickness of the transverse sections of polished specimens have been obtained using a computerized micro Vickers hardness tester.

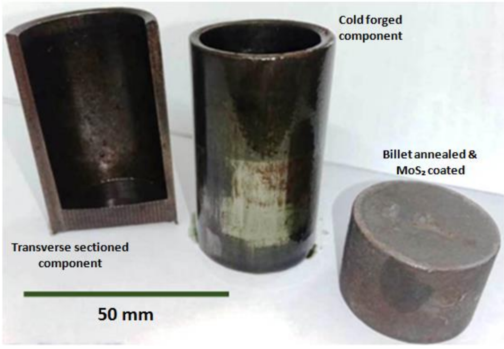

Figure 7. Billet as machined, annealed, MoS_2 coated forged, and sectioned part.

3. Results and Discussions

The forming responses of steels AISI 1010, 1018, and 1045 in cold forging backward extrusion were evaluated with ANN models, and then employed with DE optimization.

3.1. ANN Training Performance

The developed ANN model was trained with 226 input–output pattern sets and tested by utilizing the remaining 30 sets among 256 combinations. The performance of trained ANN was evaluated using Equation (9).

$$\%\ Max.\ absolute\ prediction\ error = \left| \frac{100 * (pred. - exp.)}{pred.} \right| \tag{9}$$

The maximum absolute prediction error of different steel grade ANN models for the training and testing patterns are summarized in Table 6.

Table 6. ANN training performance.

	Maximum Absolute Prediction Error (%)											
	AISI 1010				AISI 1018				AISI 1045			
	$s_{eff.}$	$\epsilon_{eff.}$	$\epsilon_{rate.}$	F	$s_{eff.}$	$\epsilon_{eff.}$	$\epsilon_{rate.}$	F	$s_{eff.}$	$\epsilon_{eff.}$	$\epsilon_{rate.}$	F
Training patterns (226)	2.22	9.98	30.15	8.53	1.89	10.81	29.08	6.18	5.24	11.99	29.16	7.75
Testing patterns (30)	3.30	13.72	29.05	5.36	11.42	8.88	24.09	4.88	1.05	8.94	27.16	4.94

3.2. Comparison of Forming Behavior of Steel

In the current investigation, the forming behavior of different AISI steels were compared with respect to the predicted forming responses; namely, effective stress, strain, strain rate, and punch force for AISI 1010, 1018, and 1045 steel using ANN models by holding input influencing factors at low, mid and higher combinations. The plots and related interpretations are presented in the following section.

3.2.1. Comparison of Forming Response: Effective Stress

The comparison of forming response–effective stress ($s_{eff.}$) for varying billet size ratios of different AISI grade steels obtained using ANN models with low, middle, and high-level combinations of a, h, and r is depicted in Figure 8. For any given combinational values of a, h, r, and z, the effective stress was significantly higher for AISI 1045, as compared to either AISI 1010 or AISI 1018. The nature of stress variations with respect to z was almost the same in all three materials for all combinational values of a, h, and r. The effective stress almost linearly increased with an increase in z up to 0.6, whereas for $z > 0.6$, the change in stress was minimum. It was also observed that the value of z at which maximum stress occurs shifts towards the origin with an increase in carbon content (max. stress for

AISI 1045 occurred at a lower z value, whereas the max. stress for AISI 1010 occurred at slightly higher *z* value). The effective stress was almost insensitive to variations in z beyond 0.6. Hence, the higher billet volume did not contribute to a rise in stress level.

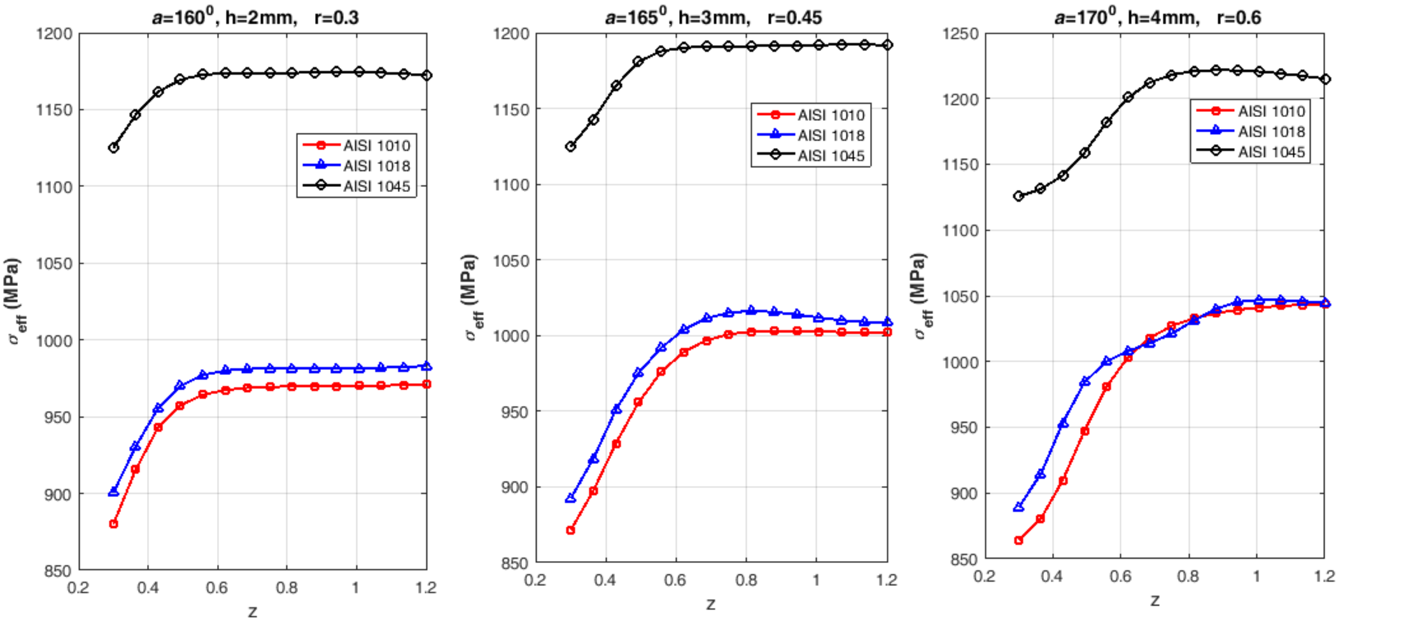

Figure 8. Comparison of forming response: effective stress.

The plots of Figure 8 eventually revealed that the increase in the carbon content of steel lowered the formability and, hence, more stress developed in the AISI 1045 steel compared to AISI 1010 and 1045. For the fixed diameter of the billet (30 mm), the punch diameter was 25 mm for r = 0.3 and 19 mm for r = 0.6; therefore, a decline in the effective stress was observed for lower to higher combinational values of a, h, and r. An increase in the volume of billet (z > 0.6) has a cushioning effect during deformation; therefore, the stress values remained unaffected or sometimes decreased for any specified combinations of a, h, and r for all three steel. However, with a lower billet length (z < 0.6), a large amount of confined volume deformed against the descending punch generating more stresses during forming.

3.2.2. Comparison of Forming Response: Effective Strain

Apparently, the effective strain ($\epsilon_{eff.}$) curves exhibited a similar phenomenon, as shown in Figure 9 for all AISI steels with given combinations of a, h, and r. However, meager deviations were observed in the strain paths among all the AISI steels.

The effective strain sharply increased with billet size ratio (z) up to around 0.7 (the effective strain was highly sensitive to z variations up to about 0.7). For all specified values of z, the strain increased with an increase in level settings of a, h, and r for all three materials. For lower combination levels of a, h, and r, the strain for AISI 1045 was slightly less than for AISI 1010 and AISI 1018 materials. For high-level settings of a, h, r, and z < 0.6, it was observed that the strain for AISI 1045 was slightly less compared to strain magnitudes for AISI 1010 and AISI 1018. However, for z > 0.6, the strain in the case of AISI 1045 was higher than either AISI 1010 or AISI 1018 materials.

The volume of metal that undergoes deformation in the region z < 0.6 is lower; hence, there is a steep increase in the values of effective strain. Contrary to this behavior, marginal variations were observed subsequently with specified combinations of a, h, and r, because of higher volume (z > 0.6) that marginally contributed to a rise in the values of effective strain. Though increased values in punch angle and land height readily increased resistance to the metal flow, observed with high-level combinations of a, h and r, actually, the effect of reduction ratio at r = 0.6 (punch diameter was 19 mm) was somewhat restrained for the fixed billet diameter. A decreased carbon content also readily assisted deformation, hence, the effective strain values were witnessed to be smaller for AISI 1045 than AISI 1010 and 1018 for all combinations of *a*, *h* and *r*. On the other hand, a dominance of AISI 1018 steel in effective strain path for higher combinations of *a*, *h*, and *r* as compared to AISI 1010 and 1045 steel, which might be correlated with a strain hardening effect that has been observed with micro-hardness values among these steel grades.

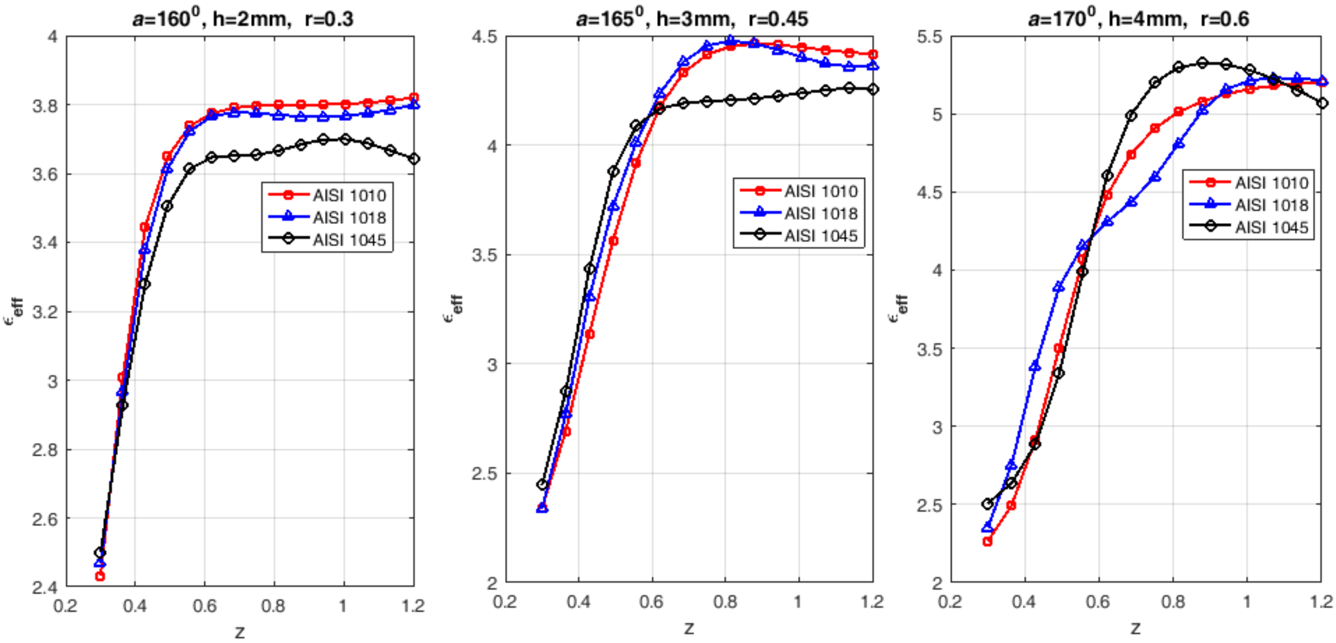

Figure 9. Comparison of forming response: effective strain.

3.2.3. Comparison of Forming Response: Effective Strain Rate

Figure 10 illustrates the rate of deformation of the AISI steels with varying billet size ratio (z) for lower, middle, and higher level combinations of *a*, *h*, and *r*. The effective strain rate (ϵ_{rate}.) was seen to be highly sensitive to level settings of *a*, *h*, and *r*. As the level settings of *a*, *h*, and *r* changed from lower to higher combinations, there was a significant reduction in the effective strain rate in all three materials tested. For $z < 0.5$, an increase in *z* results in an increased strain rate for lower settings of *a*, *h*, and *r*; while the strain rates for middle and higher settings showed a decreasing trend. Similarly, for $z > 0.5$, an increase in z resulted in a decreasing strain rate for low settings of *a*, *h*, and *r*; while the strain rate for middle and higher settings showed an increasing trend. For any specified value of *z* in the range 0.3–1.2, it was clear that lower settings of *a*, *h*, and *r* resulted in a higher strain rate.

The reduction in the effective strain rate from lower to higher combination settings of *a*, *h*, and *r* was mainly due to the punch diameter, which was changing from 25 mm ($r = 0.3$) to 19 mm ($r = 0.6$). Hence, for a 25 mm punch diameter, the deformation rate was higher, whereas it was smaller for a 19 mm diameter of punch for the same ram velocity. However, increased volume ($z > 0.6$) tended to stabilize the deformation rate for middle and higher-level combinations of *a*, *h*, and *r* because of the lower punch diameter.

3.2.4. Comparison of Forming Response: Punch Force

The plot in Figure 11 illustrates the comparison of punch force (F) values for different AISI grade steels with varying billet sizes and at specified level combinations of *a*, *h* and *r*. For all values of *z* and for all combinations of *a*, *h*, and *r*, the punch force was much more prominent in the case of AISI 1045 as compared to 1010 and 1018. For all combination settings of *a*, *h*, and *r*, the force tended to increase with an increase in *z*. For a specified value of *z*, the force tended to reduce with higher settings of *a*, *h*, and *r* in all three materials tested.

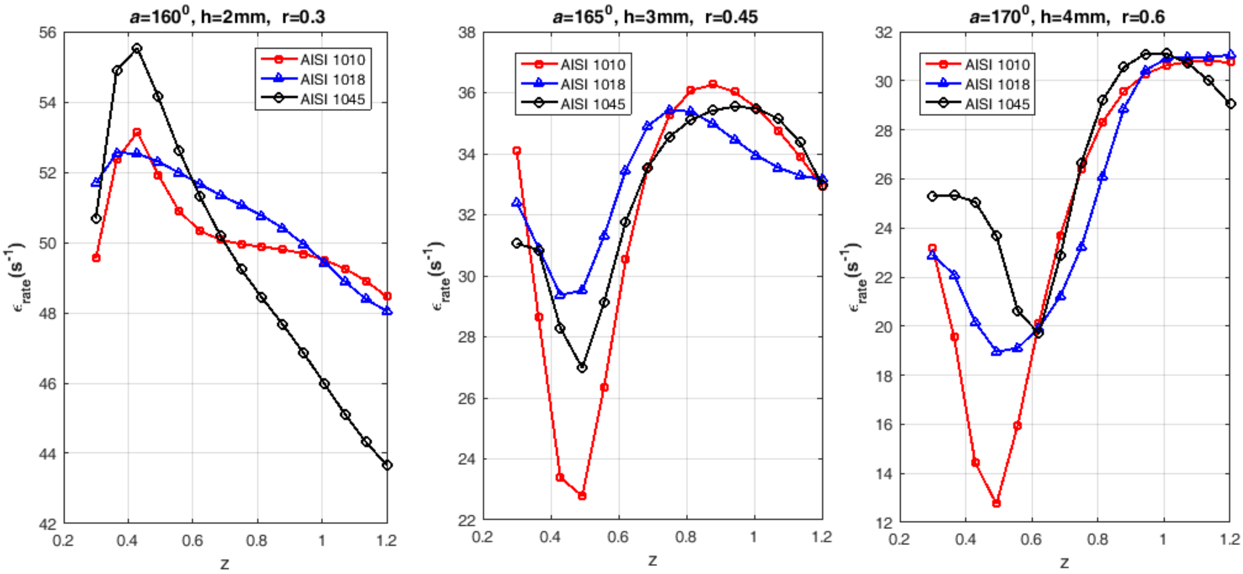

Figure 10. Comparison of forming response: effective strain rate.

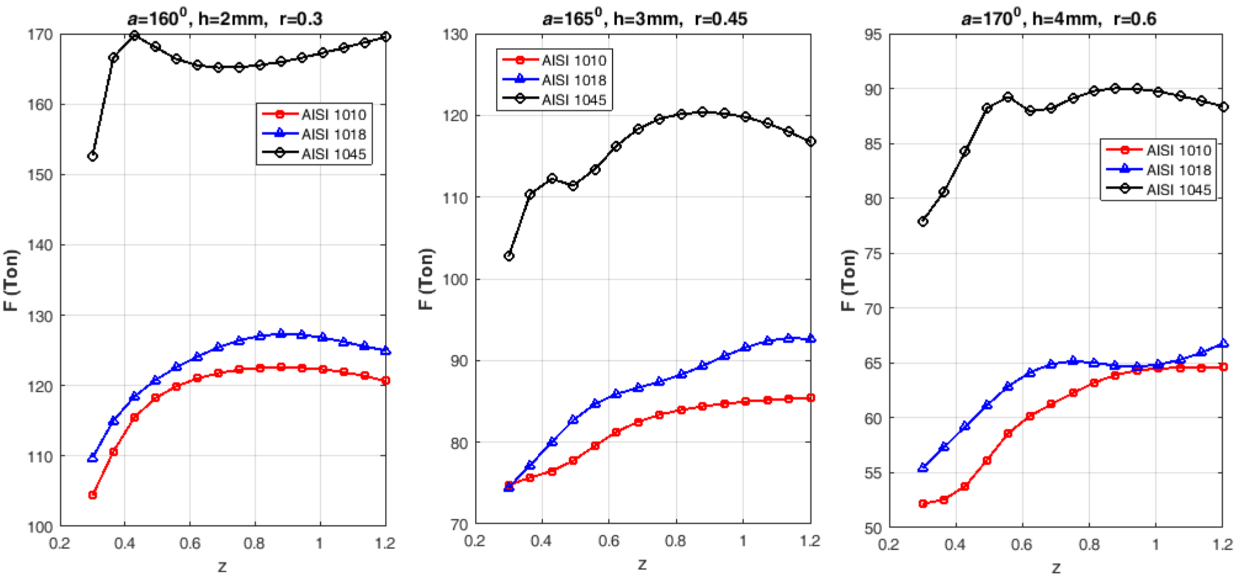

Figure 11. Comparison of forming response: punch force.

The punch force was obliviously significant for AISI 1045 than AISI 1010 and 1018 because of the increased carbon content in the steel. It is evident from the plots that increased punch angle and land height on the punch increased resistance to metal flow. However, for reduction ratio $r = 0.6$, the punch diameter was 19 mm. hence, it necessitated lower deformation force compared to $r = 0.3$ (25 mm diameter punch). An increase in the billet volume ($z > 0.6$) for fixed combinational settings of a, h, r slightly increased the punch forces for AISI 1045 due to lesser yielding, while steel with lower carbon content readily deforms, leading to the major rise in punch force.

The plots shown in Figures 8–11, derived from the ANN models for forming responses of AISI 1010, 1018, and 1045, revealed the formability nature of the different AISI grade steels. The forming responses were observed to be majorly affected by the reduction ratio, whereas, the marginal influence of the punch angle and land height was witnessed. However, punch angle and land height were major concerns in deciding the service life of the punches in cold forging backward extrusion. The consequence of the billet size ratio was clearly visible in the range of 0.3 to 0.6, and a further increase in the volume merely increased the values of the forming responses. The deformation was also primarily affected by the carbon content of the steel, as evidenced by AISI 101, 1018, and 1045 steel.

From the above response analysis, it is clear that the relationship between various responses and chosen process parameters was highly non-linear and, hence, ANN modeling is appropriate as compared to other modeling approaches, such as response surface methods.

3.3. Analysis of DE Optimization Parameters

The DE optimization technique enables arriving at the optimal combinations to achieve the objective of minimizing the response variables. The billet size ratio (z), reduction ratio (r) were maintained as independent parameters with practical intuition for which the optimal values of punch face angle (a-deg) and land height (h-mm) were determined for AISI 1010, 1018, and 1045 steel.

The optimal punch angle at different reduction and billet size ratios for AISI steels is illustrated in Figure 12. The optimal punch angle obtained through the DE technique was 170° for r = 0.3 for AISI 1010, 1018, and 1045, irrespective of the billet size ratio. However, the optimal punch angle was leaning towards 160° until approximately z = 0.6 and reversed thereafter for different AISI grades steel. The optimal punch angle was also observed to be striding to 170° for AISI 1045 rather than 1010 and 1018 for the given reduction and billet size ratio, substantiating the effect of carbon content in the cold forging process of various steels.

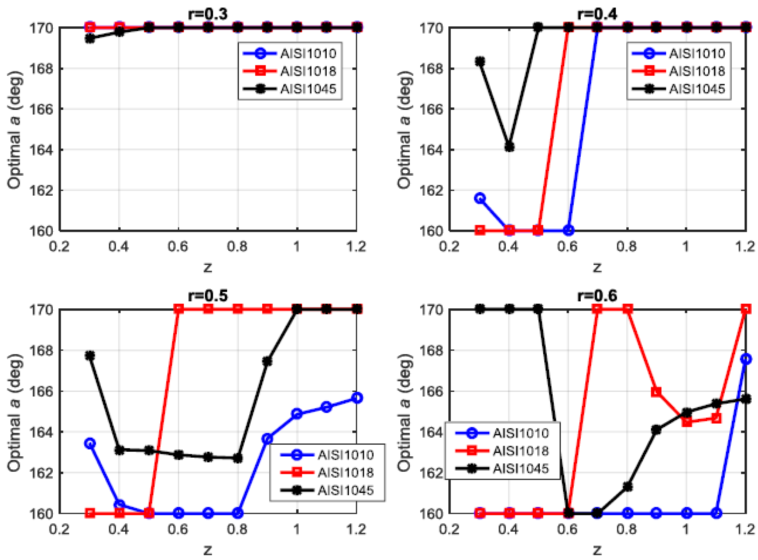

Figure 12. Comparison of optimal values of punch face angle (a) for different steels.

Subsequently, optimal land height (h) values for different reduction ratios with varying billet size ratios for AISI 1010, 1018, and 1045 steel have been plotted in Figure 13. A similar trend was witnessed for optimal land height on the punch, where the optimal land height values were seen to be close to 4 mm for low carbon steel and descended to 2 mm for AISI 1045 steel. The reason was probably because of friction during metal flow and contact conditions during cold forming.

Comparison of Steel for Optimal Response Factors

The optimal combinations of control factors, billet size ratio (z), reduction ratio (r), punch angle (a), and land height (h), obtained from the DE technique have resulted in the optimal responses for effective stress, strain, strain rate, and punch force. The optimal forming responses were compared through plots generated by keeping the billet size (z) and reduction ratios (r) as independent input variables.

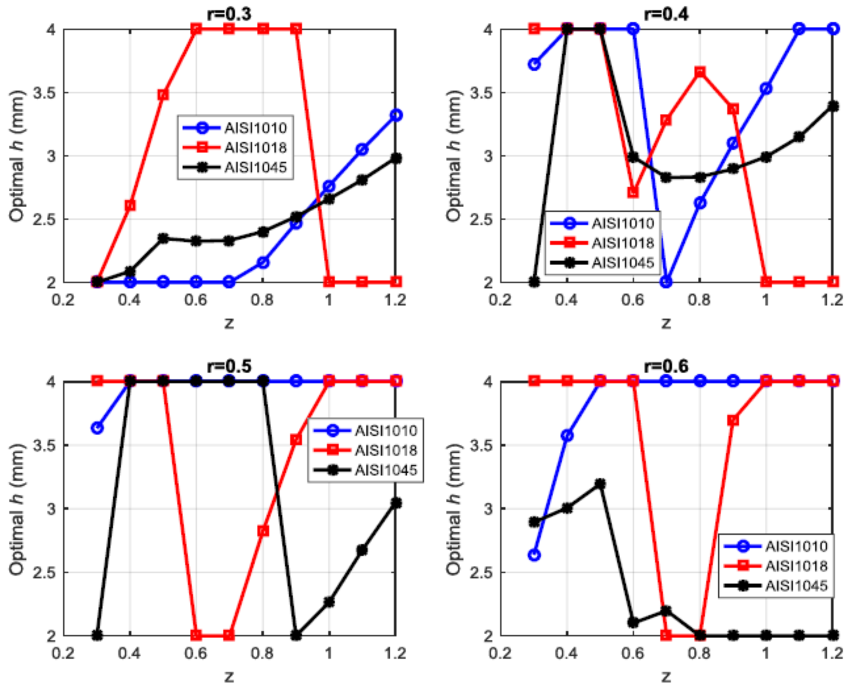

Figure 13. Comparison of optimal values of land height (*h*) of different steels.

- Optimal response factor comparison: effective stress

The optimal effective stress $\left(\sigma_{eff.}\right)$ curves for the reduction ratios (*r* = 0.3, 0.4, 0.5, and 0.6) with varying billet size ratio (*z*) from 0.3 to 1.2 was observed to be increased until *z* = 0.6 and further remained almost stagnant thereafter, up to *z* = 1.2 for all steel grades, as illustrated in Figure 14. However, it is evident from the plots that though the optimal effective stress trend was similar for AISI 1010, 1018, and 1045 steels; the stress values increased with varying carbon content. It was also apparent that the effective stress values for the particular grade steel was slightly increased with reduction ratio, while, overall, there was little variation in between AISI1010 and AISI1018 as compared to AISI 1045. This 2 to 4% deviation observed was probably due to the carbon presence in the steel, which largely dictated the formability. The AISI 1045 steel contains a larger % of carbon than the other two AISI grade steels.

- Optimal response factor comparison: effective strain

Since the amount of deformation remained similar for different steel grades for the given billet size and reduction ratio, there was marginal deviation observed in the plots of the optimal effective strain among AISI steels, as shown in Figure 15. However, optimal effective strain values were increased with a billet size ratio (*z*) up to 0.6 for all steel grades; subsequently, no significant rise was observed. The optimal effective strain values for AISI 1045 were slightly leading until *z* = 0.6 and marginally held-back until *z* = 1.2 compared to that of AISI 1010 and 1018 steel, possibly because of residue elasticity that affects more with volume.

- Optimal response factor comparison: effective strain rate
- Optimal response factor comparison: punch force

The optimal response-punch force for optimal control factors obtained by the DE technique with varying reduction ratios is shown in Figure 17. The optimal punch force values have been observed to be considerably larger for AISI 1045 compared to AISI 1010 and 1018 with all cases of reduction ratios. However, slight variations are seen in the optimal punch values of AISI 1010 and 1018 because of differences in percentage carbon compositions in these alloys. An increase in billet volume beyond *z* = 0.6 marginally affects the optimal punch force, whereas an increasing trend was seen in the region *z* < 0.6.

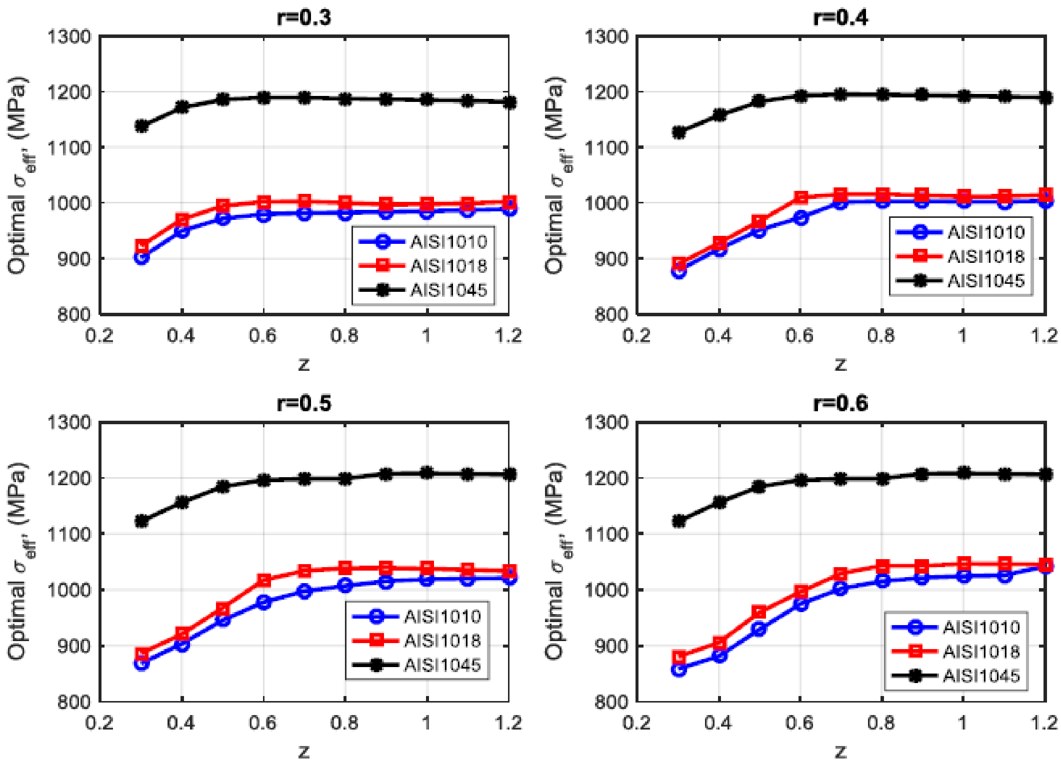

Figure 14. Comparison of optimal values of effective stress of different steels.

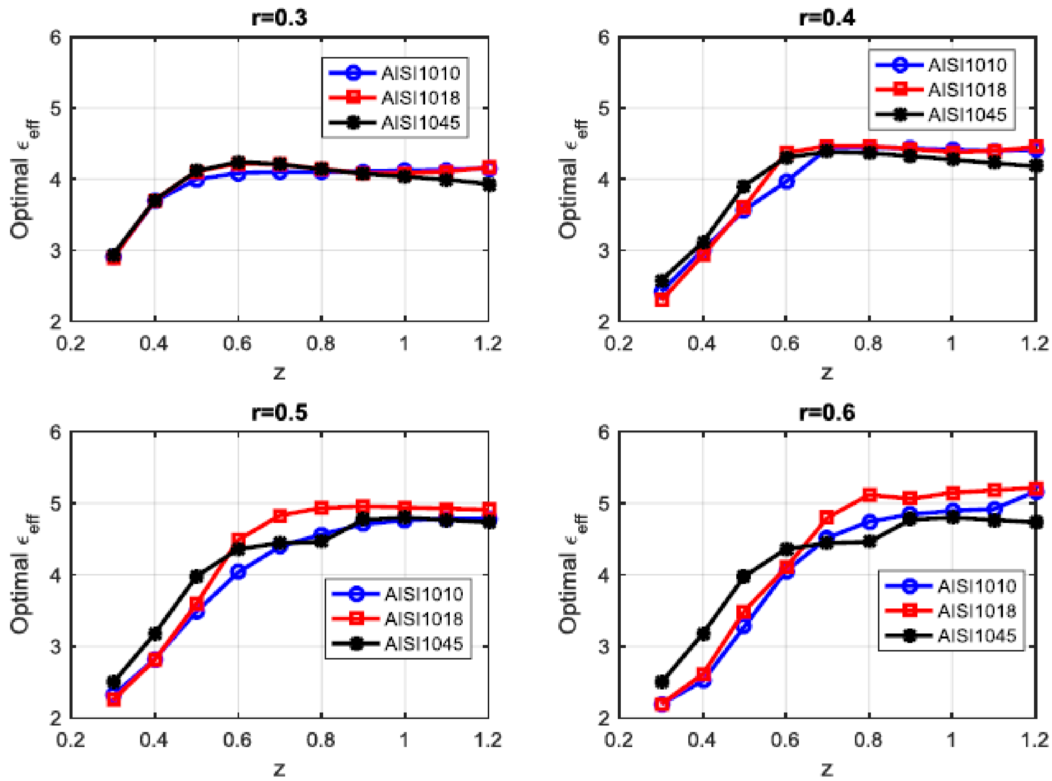

Figure 15. Comparison of optimal values of the effective strain of different steels.

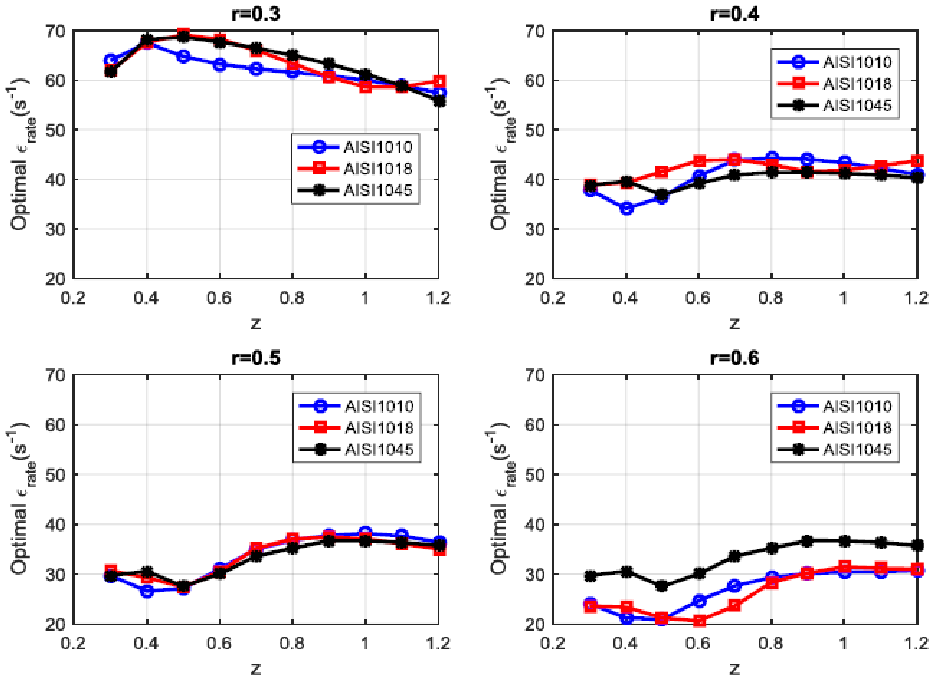

Figure 16. Comparison of optimal values of effective strain rate of different steels.

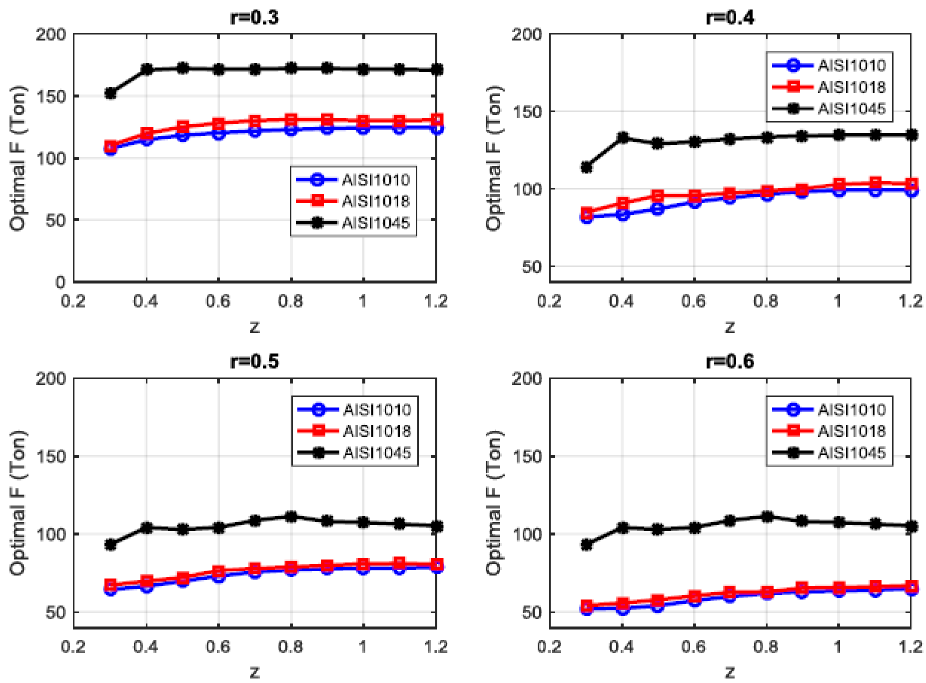

Figure 17. Comparison of optimal values of punch force of different steels.

3.4. Experimental Validation

The responses of eight representatives of DE optimal combinations were acquired during the experiments, such that a minimum of five replicates (forgings) in each combination were tested and averaged. A good correlation was witnessed between the experimental values and DE optimal responses.

3.4.1. Punch Force Estimation

The force was directly captured with a master force gauge coupled with the main hydraulic press line through a digital single-lens reflex camera. Figure 18 illustrates the comparison between average readings on the dial during experiments and corresponding DE optimal punch force values.

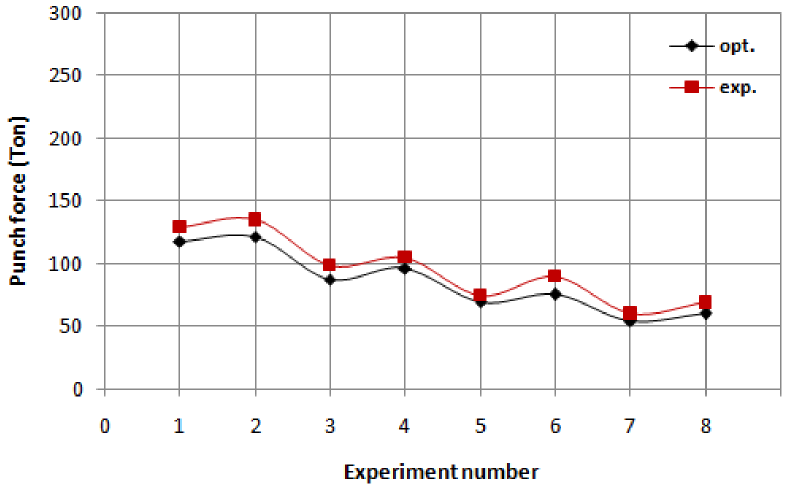

Figure 18. Comparison of DE optimal and experimental values for punch force.

Optimal Values for the punch force show an excellent resemblance to gauge readings obtained from experiments. However, the punch force acquired through the master gauge seems to be on the higher side, probably because of the presses' frictional losses and the hydraulic line [37,38]. Moreover, the deviations lie within 10% but could be justifiable with the available conventional technique adopted to capture the readings. The punch diameter was 19 mm for $r = 0.6$. Hence, the punch force was observed to be decreased with increasing reduction ratio. It was also observed that the punch force was affected by the billet size ratio z; the punch force increased with z, as illustrated in Figure 19. The billet diameter was 30 mm, and the length was varied to accommodate the billet size ratio z (billet length to diameter ratio) in the range of 0.3–1.2. As the billet length increased from 15 mm ($z = 0.5$) to 21 mm ($z = 0.7$), more volume underwent deformation and hence, increased punch force.

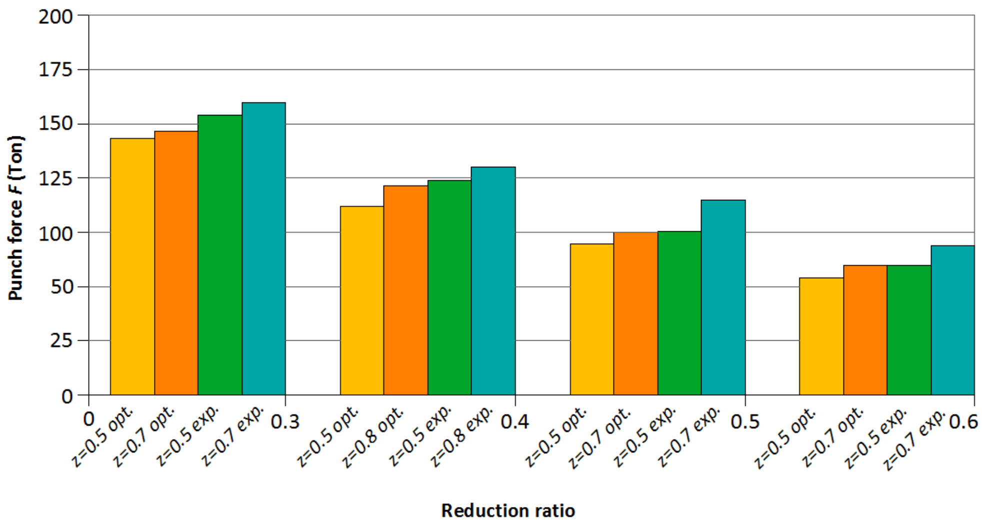

Figure 19. Variation between optimal and experimental values of punch force at different reduction ratios.

3.4.2. Effective Strain and Stress Estimation

The ductility of a billet material is essential for the evaluation of material behavior in forming applications because it determines the limits of plastic deformations. In addition, the cold forging backward extrusion process is most suitable option for forming moderately ductile materials. For the estimation of effective stress experimentally, the deformation or the strain was determined during the cold forging process. An analytical model comprising a slab and power analysis was implemented to evaluate the effective strain. The three-zone model is presented in Figure 20a and has been an acceptable choice to describe the forming behavior during cold forging backward extrusion.

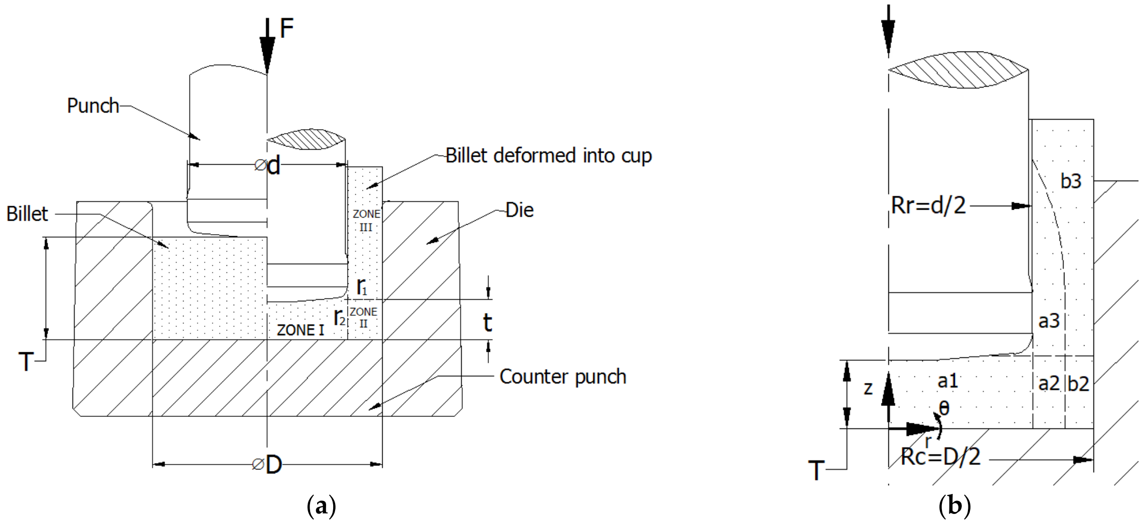

Figure 20. (**a**) Three-zone representation of the cold forging backward extrusion process. (**b**) Strain distribution areas for the three-zone representation.

As shown in Figure 20a, plastic deformation is represented by the first and second zones, while, the third zone is the rigid one. These are separated by the surface of discontinuity r_1 and r_2. The process geometry is described by punch diameter Ød, die diameter ØD, current bottom thickness t, and billet thickness T [39].

Dipper [40] proposed effective strain as a measure of deformation for zone I and zone II with Equations (10) and (11), respectively, whereas zone III is free from stresses. The equivalent strain distribution is evaluated as a function of punch position into the billet and found to be large in zone II. Sillekens [41] compiled excerpts on effective strain distribution in backward extrusion with a set of algorithms. The distribution zones in the backward extruded cup are depicted in Figure 20b.

$$\epsilon_{eff.zone\ I} = ln\left(\frac{T}{t}\right) \tag{10}$$

$$\epsilon_{eff.zone\ II} = ln\left(\frac{T}{t}\right).\left[1 + \frac{d}{4 \times (D-d)}\right] \tag{11}$$

The comparison of the effective strain distribution obtained by experimentation showed good agreement with the values obtained from DE optimization, as evident from the plot in Figure 21.

The effective stress can be estimated using the following Equation (12) with the strain values obtained from experimentation.

$$\sigma_{eff.} = \mathrm{K}(\varepsilon)^n \tag{12}$$

where n—strain-hardening exponent and K—strength coefficient.

The values of constants K and n for AISI 1010 material are 715.67 MPa and 0.22, respectively, and a comparison is shown in Figure 22 [28].

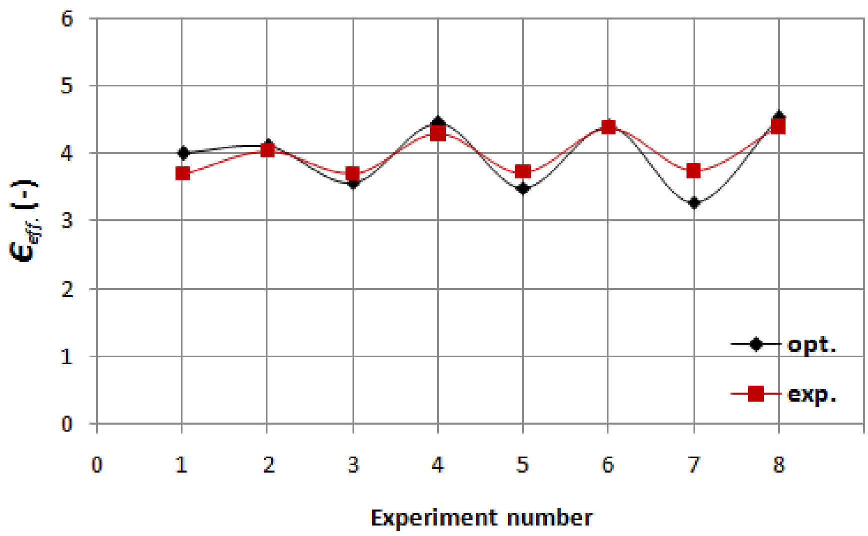

Figure 21. Comparison of DE optimal and experimental values for effective strain.

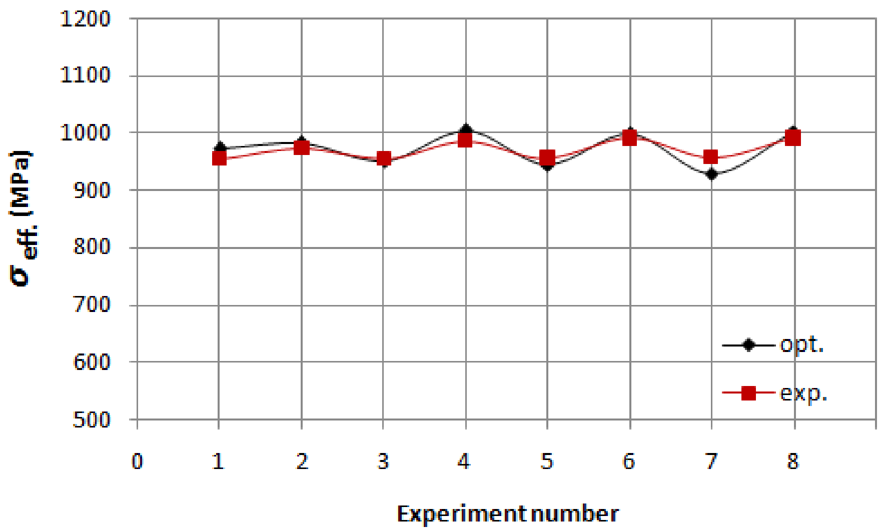

Figure 22. Comparison of DE optimal and experimental values for effective stress.

3.4.3. Effective Strain Rate Estimation

The strain rate is a measure of deformation with respect to time and an essential aspect in deciding on the cycle time of cold forging [29]. During the cold forging process, the punch forces the billet into the die, and as the forces exceed, the billet material starts deforming plastically. The process video footage captured is segmented for the entire stroke cycle duration and visually examined to record the punching time span.

The effective strain rate values are obtained by multiplying the time elapsed during forging with the calculated experimental strain values. The marginal deviation is observed in the effective strain rate between experimental and DE optimal values, as shown in Figure 23. The press ram stroke might not have constant speed throughout the stroke practically (though set properly) because of inherent attributes depending on the machine condition, such as mechanical backlash and hydraulic line frictional losses that lead to a decrease in the stroke speed significantly once the billet comes into contact with the punch.

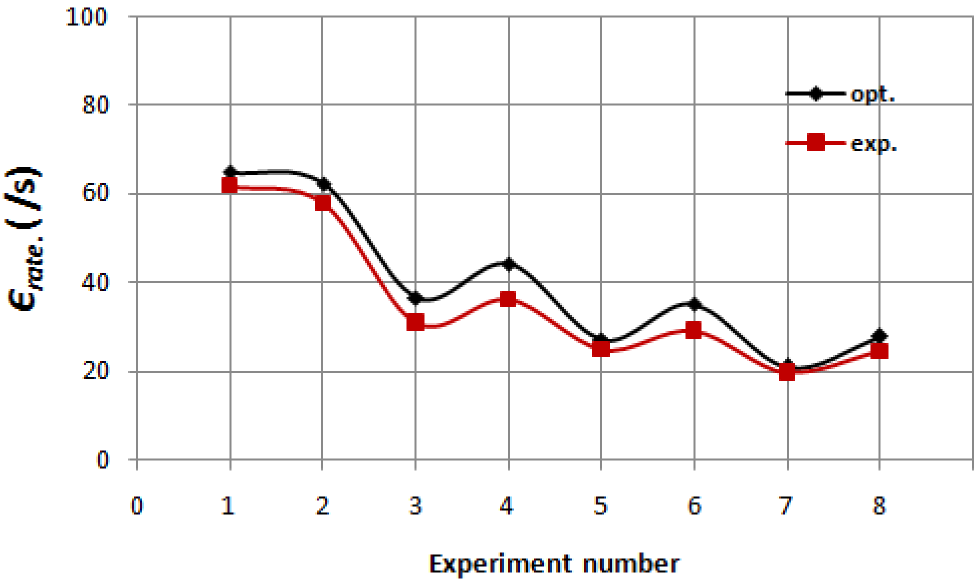

Figure 23. Comparison of DE optimal and experimental values for effective strain rate.

3.5. Microstructural Observation

The surfaces of cold forging backward extrusion samples of AISI 1010, AISI 1018, and AISI 1045 were prepared with standard metallographic techniques. Then, surfaces were etched with NITTAL solution and the microstructure was examined with a scanning electron microscope (SEM). The consequence of cold forging was viewed on the surface, in transverse section. The grain structure of the forged component was analyzed closely with two magnification levels and reported in Figure 24.

Upon cold forging backward extrusion, the initial coarse-grained microstructure characterized by uniform dispersion with globules layout (because of annealing treatment) were transformed into fine grains elongated in the direction normal to the forging and can be attributed to the severe plastic deformation. The microstructure of the transverse section of the forged component of AISI 1010, AISI 1018, and AISI 1045 from Figure 24, shows the traces of refined grain that are closely packed with no signs of cracks. In contrast, mechanical integrity and uniformity are preserved along grain boundaries; clearly confirming the non-separation of grains and distortion through plastic deformation in the applied strain direction. The microstructural examinations reveal the mechanical soundness of the components produced from AISI 1010, AISI1018, and AISI 1045 and the aptness of the identified geometrical attributes.

The micro-hardness values were obtained for the transverse section of the forged specimen of AISI 1010, AISI 1018, and AISI 1045 by a Vicker's computerized micro-hardness tester. Figure 25 indicates the average micro-hardness measured on the samples of the billets as machined, annealed, and as a forged condition of AISI 1010, AISI1018, and AISI 1045 steel. It is apparent from the plot that the Vicker's value was 267 for AISI 1018, comparatively more than AISI 1045 and AISI 1010 for the forged samples. The AISI 1018 steel being low-medium carbon steel was observed to be highly responsive to the cold forming process, as evidenced by the Vickers hardness, and substantiated the steel's ability to be implemented in the production of automotive components featured with good process-induced mechanical strength.

From the above analysis of forming behavior for different grades of steel in cold forging, it is evident that the ANN has the potential to capture a non-linearity with admirable generalization with reasonable precision. The parameters selected for ANN training and the validation were acquired by a number of simulations and found to be proper for modeling the identified geometrical attributes. In addition, DE optimization results disclosed that for every geometrical attribute, the optimal state of forming responses is different for every grade of steel. There exist several optimal solutions since the association among the planned forming behavior and the selected variables was highly complex and non-linear. The results of DE optimization presented here represent one such possible optimal solution obtained through the designed fitness function.

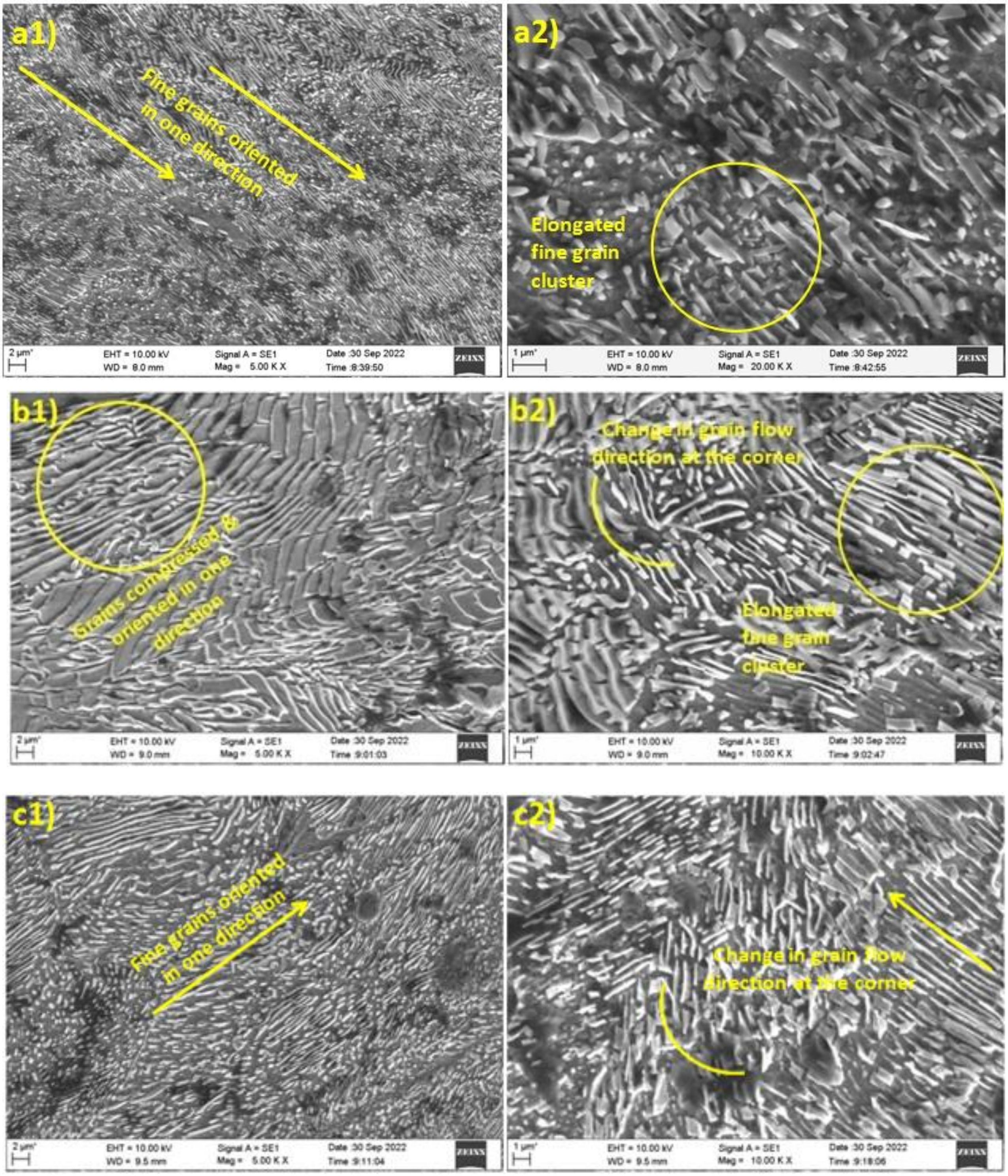

Figure 24. Microstructure of AISI steels. (**a1**,**a2**) AISI 1010; (**b1**,**b2**) AISI 1018; (**c1**,**c2**) AISI 1045.

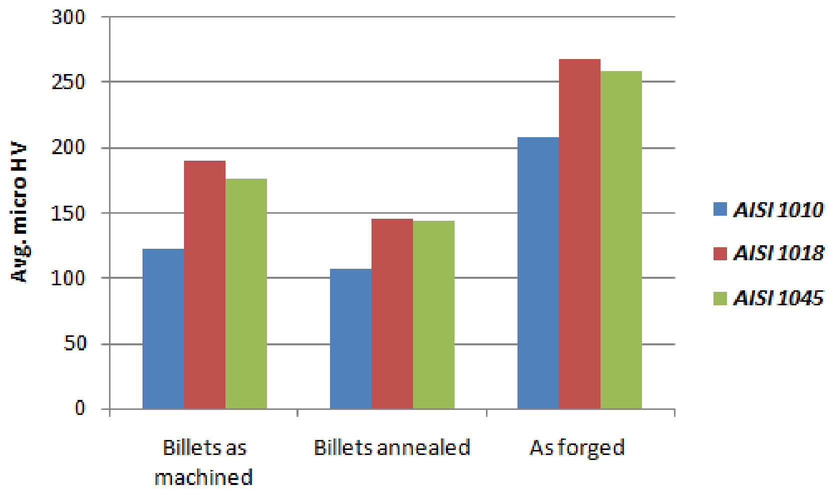

Figure 25. Comparison of micro-hardness values for AISI steels.

4. Conclusions

The application of differential evolution (DE) optimization for minimizing the forming responses, such as effective stress, strain, and punch force, while maximizing the strain rate has been presented in this paper. The geometrical attributes such as billet size, reduction ratio, punch angle, and land height that significantly affect cold forging backward extrusion of different steels, namely AISI 1010, 1018, and 1045, have been optimized. The fitness function was designed by mapping the forming responses for DE optimization. The forming responses were recorded through FE simulations and the models required for DE optimization were developed using artificial neural network (ANN), which were strategically planned according to full factorial experimental design (FFD). The error back propagation training algorithm (EBPTA) has been employed for ANN modeling. Following are the observations made through our investigation.

- The forming responses are observed to be majorly affected by the reduction ratio, whereas, the marginal influence of the punch angle and land height is witnessed. However, punch angle and land height are major concerns in deciding the service life of the punches in cold forging backward extrusion. The effect of the billet size ratio is seen in the range from 0.3 to 0.6, and a further increase in the volume merely increases the values of forming responses. The deformation is also largely affected by the carbon content of the steel, as evidenced by AISI 1010, 1018, and 1045 steel materials.
- The optimal punch angle for a reduction ratio of 0.3 is at 170° irrespective of the billet size ratio and type of AISI grade chosen steels tested. However, the punch angle is highly susceptible to the carbon content of the steel, reduction, and billet size ratio. Similarly, optimal land height is found to be closer to around 4 mm for AISI 1010 and 1018, whereas minimal (about 2 mm) for AISI 1045 for the increased reduction and billet size ratios. Hence, it is clear that steel's formability is majorly affected by the steel's carbon content, while land height and punch angle are decided based on the internal profile of the component and has a bearing upon punch service life.
- Effective stress and strain optimal values obtained from optimization were observed to be of a similar trend and increased with reduction and billet size ratios. However, effective strain and punch force optimal values were reported to increase with decreased reduction ratios and remain marginally affected by billet size ratios. For the estimation of effective stress experimentally, the deformation or the strain is determined during cold forging and an analytical model comprising of the slab and power analysis has been implemented to arrive at the effective stress. The effective stress and strain values from experiments and those from the FE simulation and DE method are in good agreement.

- The cold forging backward extruded components have also been examined for better mechanical soundness, which eventually confirms the appropriateness of the identified variables. The microstructural observations for forged parts split in transverse sections revealed directionally oriented grain refinement. The micro-hardness along the transverse section for the cold forging backward extruded AISI grade steels were analyzed and it was observed that the average micro-hardness value of AISI 1018 was 267 Hv when comparatively higher than AISI 1010 and AISI 1045 steels. However, the cold forging backward extrusion resulted in an overall increase in average hardness and might be attributed to the fact that cold forging backward extrusion complies with the production of superior parts with good strength.

Author Contributions: Conceptualization, P.M.P. and V.N.G.; methodology, P.M.P. and V.N.G.; software, R.S.K. and P.M.P.; validation, V.N.K. and J.P.D.; formal analysis, P.M.P. and R.S.K.; investigation, P.M.P.; resources, V.N.K. and V.N.G.; data curation, P.M.P., R.S.K. and V.N.G.; writing—original draft preparation, P.M.P., V.N.G. and V.N.K.; writing—review and editing, J.P.D. and R.S.K.; visualization, P.M.P. and V.N.K.; supervision, V.N.G. and R.S.K.; project administration, V.N.G. and J.P.D. All authors have read and agreed to the published version of the manuscript.

Funding: This research received no external funding.

Institutional Review Board Statement: Not Applicable.

Informed Consent Statement: Not Applicable.

Data Availability Statement: This study did not report any data.

Acknowledgments: The authors would like to express their gratitude and special thanks to KLE Technological University, Hubballi, India, for sanctioning capacity-building funds (CBF) to carry out the project. The entire work has been carried out under the CBF for the years 2021–2022. The authors would like to thank the technical staff of S. S. Industries, Bangalore, India for supporting their experimental work.

Conflicts of Interest: The authors declare no conflict of interest.

References

1. Altan, T.; Ngaile, G.; Shen, G. *Cold and Hot Forging: Fundamentals and Applications*; ASM International: Almere, The Netherlands, 2004; Volume 1.
2. Meidert, M.; Hänsel, M. Net shape cold forging to close tolerances under QS 9000 aspects. *J. Mater. Process. Technol.* **2000**, *98*, 150–154. [CrossRef]
3. Marini, D.; Cunningham, D.; Corney, J.R. Near net shape manufacturing of metal: A review of approaches and their evolutions. *Proc. Inst. Mech. Eng. Part B J. Eng. Manuf.* **2018**, *232*, 650–669. [CrossRef]
4. Arreola-Herrera, R.; Cruz-Ramírez, A.; Suárez-Rosales, M.; Sánchez-Álvarado, R.G. The effect of cold forming on structure and properties of 32 CDV 13 steel by radial forging process. *Mater. Res.* **2014**, *17*, 445–450. [CrossRef]
5. Gronostajski, Z.; Hawryluk, M. The main aspects of precision forging. *Arch. Civ. Mech. Eng.* **2008**, *8*, 39–55. [CrossRef]
6. Sun, M.C.; Tzou, G.Y.; Zheng, L.A. Study on multi-stage cold forging of stainless automotive battery fastener. In *Applied Mechanics and Materials*; Trans Tech Publications Ltd.: Wollerau, Switzerland, 2013; Volume 284, pp. 211–215.
7. Kosec, B.; Brezigar, M.; Kosec, G.; Bernetic, J.; Bizjak, M. Heat treatment of cold formed steel forgings for the automotive industry. *J. Achiev. Mater. Manuf. Eng.* **2007**, *22*, 87–90.
8. Ku, T.-W.; Kim, L.-H.; Kang, B.-S. Multi-stage cold forging and experimental investigation for the outer race of constant velocity joints. *Mater. Des.* **2013**, *49*, 368–385. [CrossRef]
9. Min, D.-K.; Kim, M.-E. A study on precision cold forging process improvements for the steering yoke of automobiles by the rigid–plastic finite-element method. *J. Mater. Process. Technol.* **2003**, *138*, 339–342. [CrossRef]
10. Khaleed, H.M.T.; Samad, Z.; Othman, A.R.; Mujeebu, M.A.; Arshad, M.R.; Ab-Kadir, A.R.; Hussaini, M.A.; Abdullah, A.B. Finite element analysis and experimental validation of flashless cold forging of propeller hubs and blade of autonomous underwater vehicle. *Proc. Inst. Mech. Eng. Part B J. Eng. Manuf.* **2010**, *224*, 1455–1467. [CrossRef]
11. Yoon, J.; Jeon, H.; Lee, J. Process design of cold forging with thick plate for seat recliner parts. *Mater. Des.* **2013**, *49*, 449–455. [CrossRef]
12. Engel, U.; Groenbaek, J.; Hinsel, C.; Kroiß, T.; Meidert, M.; Neher, R.; Schrader, T. *Tooling Solutions for Challenges in Cold Forging*; Eder, W.K., Ed.; UTF Science: Bamberg, Germany, 2011.
13. Vazquez, V.; Hannan, D.; Altan, T. Tool life in cold forging–an example of design improvement to increase service life. *J. Mater. Process. Technol.* **2000**, *98*, 90–96. [CrossRef]

14. Handbook, M. American Society for Metals. In *Forming and Forging*; ASM International: Novelty, OH, USA, 1996; Volume 14, pp. 1376–1400.
15. Barišić, B.; Ungureanu, N.; Car, Z. Investigation of Forming Force at Backward Extrusion Process on Different Aluminum Materials. *Sci. Bul. Ser. C* **2008**, *22*, 21–27.
16. Ebara, R.; Takeda, K.; Ishibashi, Y.; Ogura, A.; Kondo, Y.; Hamaya, S. Microfractography in failure analysis of cold forging dies. *Eng. Fail. Anal.* **2009**, *16*, 1968–1976. [CrossRef]
17. MacCormack, C.; Monaghan, J. Failure analysis of cold forging dies using FEA. *J. Mater. Process. Technol.* **2001**, *117*, 209–215. [CrossRef]
18. Yang, D.Y.; Kim, Y.U.; Lee, C.M. Analysis of center-shifted backward extrusion of eccentric tubes using round punches. *J. Mater. Process. Technol.* **1992**, *33*, 289–298. [CrossRef]
19. Mori, T.; Li, S. A new definition of complexity factor of cold forging process. *Precis. Eng.* **2009**, *33*, 44–49. [CrossRef]
20. Kaur, J.; Pabla, B.S.; Dhami, S.S. A review on field areas of research in forging process using FEA. *Int. J. Eng. Res. Technol.* **2016**, *5*, 383–393.
21. Ryu, C.H.; Joun, M.S. Finite element simulation of the cold forging process having a floating die. *J. Mater. Process. Technol.* **2001**, *112*, 121–126. [CrossRef]
22. Khaleed, H.M.T.; Samad, Z.; Othman, A.R.; Mujeebu, M.A.; Abdullah, A.B.; Zihad, M.M. Work-piece optimization and thermal analysis for flash-less cold forging of AUV propeller hubs—FEM simulation and experiment. *J. Manufac.-Turing Process.* **2011**, *13*, 41–49. [CrossRef]
23. Jun, B.Y.; Kang, S.M.; Lee, M.C.; Park, R.H.; Joun, M.S. Prediction of geometric dimensions for cold forgings using the finite element method. *J. Mater. Process. Technol.* **2007**, *189*, 459–465. [CrossRef]
24. Sedighi, M.; Hadi, M.; Kolahdouz, S. Optimization of Preform in Close Die Forging by Combination of Neural Network and Genetic Algorithm 1. *World Appl. Sci. J.* **2009**, *7*, 1464–1473.
25. Ciancio, C.; Citrea, T.; Ambrogio, G.; Filice, L.; Musmanno, R. Design of a high performance predictive tool for forging operation. *Procedia CIRP* **2015**, *33*, 173–178. [CrossRef]
26. Ku, T.W. A study on two-stage cold forging for a drive shaft with internal spline and spur gear geometries. *Metals* **2018**, *8*, 953. [CrossRef]
27. Ku, T.-W. A Combined Cold Extrusion for a Drive Shaft: A Parametric Study on Tool Geometry. *Materials* **2020**, *13*, 2244. [CrossRef] [PubMed]
28. Bringas, J.E. *Handbook of Comparative World Steel Standards*, 3rd ed.; ASTM International: West Conshohocken, PA, USA, 2004.
29. Petkar, P.M.; Gaitonde, V.N.; Karnik, S.R.; Kulkarni, V.N.; Raju, T.K.G.; Davim, J.P. Analysis of Forming Behavior in Cold Forging of AISI 1010 Steel Using Artificial Neural Network. *Metals* **2020**, *10*, 1431. [CrossRef]
30. Montgomery, D.C. *Design and Analysis of Experiments*; John Wiley & Sons. Inc.: New York, NY, USA, 1997; pp. 200–201.
31. Planchard, D. *SOLIDWORKS, Tutorial with Video Instruction*; SDC Publications: Mission, KS, USA, 2018.
32. Joun, M. Recent Advances in Metal Forming Simulation Technology for Automobile Parts by AFDEX. *IOP Conf. Ser. Mater. Sci. Eng.* **2020**, *834*, 012016. [CrossRef]
33. Schalko, R.B. *Artificial Neural Networks*; McGraw-Hill: Singapore, 1997.
34. MATLAB. *MATLAB NN Toolbox*; Math Works Incorporation: Natick, MA, USA, 2016.
35. Ahmad, M.F.; Isa, N.A.M.; Lim, W.H.; Ang, K.M. Differential evolution: A recent review based on state-of-the-art works. *Alex. Eng. J.* **2021**, *61*, 3831–3872. [CrossRef]
36. Kulkarni, V.N.; Gaitonde, V.N.; Karnik, S.R.; Manjaiah, M.; Davim, J.P. Machinability analysis and optimization in wire EDM of medical grade NiTiNOL memory alloy. *Materials* **2020**, *13*, 2184. [CrossRef]
37. Kroiß, T.; Engel, U.; Merklein, M. Comprehensive approach for process modeling and optimization in cold forging considering interactions between process, tool and press. *J. Mater. Process. Technol.* **2013**, *213*, 1118–1127. [CrossRef]
38. Krušič, V.; Arentoft, M.; Mašera, S.; Pristovšek, A.; Rodič, T. A combined approach to determine workpiece-tool-press deflections and tool loads in multistage cold-forging. *J. Mater. Process. Technol.* **2011**, *211*, 35–42. [CrossRef]
39. Miłek, T. The analysis of distributions of effective strain and flow stress in longitudinal sections of cold backward extruded copper cans for different punch-face shapes. *ITM Web Conf.* **2017**, *15*, 07014. [CrossRef]
40. Dipper, M. Das Fließpressen von Hülsen in Rechnung und Versuch. *Arch. Eisenhüttenwes.* **1949**, *20*, 275–286. [CrossRef]
41. Sillekens, W.H. *Backward Can Extrusion and Materials Behavior*; Technische Universiteit Eindhoven: Eindhoven, The Netherlands, 1992.